Supplementary Information for

Dampening of expression oscillations by synchronous regulation of a microRNA and its target

Dong hyun Kim, Dominic Grün & Alexander van Oudenaarden

Supplementary Note

Derivation of steady-state model and analytical understanding of the miR-IFFL performance

We built a mathematical model to characterize the dynamics of target gene level u in the presence of miRNA level m (Supplementary Fig. 13b). We assumed a time-variant production of the target mRNA $k_R(t)$ and miRNA $k_m(t)$, with decays described by first-order constant rates γ_R and γ_m respectively. We also assumed irreversible second-order miRNA-mediated target transcript degradation kinetics with a rate constant k_{on}. The rate k_{on} depends on the strength of the miRNA-target interaction which is proportional to the number of miRNA complementary elements N of the target transcript (thus $k_{on}(N=0) = 0$ in both *lin-4(e912)* and *lin-14(n355gf)* strains).

$$\dot{u}(t) = k_R(t) - k_{on} \cdot u(t) \cdot m(t) - \gamma_R \cdot u(t)$$

$$\dot{m}(t) = k_m(t) - \gamma_m \cdot m(t)$$

We directly used the *lin-14* mRNA concentration of *lin-14(n355gf)* animals (smoothened by local regression and body length (µm) transformed into units of time (hrs)) to infer $u(t)$ and $\dot{u}(t)$ to derive $k_R(t, \gamma_R)$ given that $k_{on}(N = 0) = 0$ for this strain. To find $m(t)$, we used our spline-fitted experimental measurement of mature lin-4 from *lin-14(n355gf)* animals (Supplementary Fig. 13f). With $k_R(t, \gamma_R)$ and $m(t)$, we fitted our time dependent model of $u(t)$ to our experimental data for $N = 7$ (wild-type) and $N = 2$ (*lin-14(n536gf)*) (again, smoothened by local regression and body length (µm) transformed into units of time (hrs)) to obtain k_{on} and γ_R that gave the best fit values.

By computing the sum of squares of the fit for a range of k_{on} and γ_R, we found that sum of squares of the fit to be minimized when the ratio $\dfrac{k_{on}}{\gamma_R}$ carried a certain constant value, and not to depend on individual values of k_{on} and γ_R (Supplementary Fig. 13c,d). We speculated that such

redundancy in the fit parameter space was due to an over-fitting of our time-dependent model to the experimental data. This led us to reduce our time-dependent model to a steady-state model.

Assuming that the *lin-14* mRNA concentration is in steady-state, we find a simple analytical expression for steady state *lin-14* mRNA concentration $u_{st}(t)$

$$0 = \dot{u}(t) = k_R(t) - k_{on} \cdot u_{st}(t) \cdot m(t) - \gamma_R \cdot u_{st}(t)$$

$$0 = \dot{m}(t) = k_m(t) - \gamma_m \cdot m(t)$$

$$\Rightarrow u_{st}(t) = \frac{k_R(t)/\gamma_R}{1 + \alpha \cdot m(t)} \qquad [1]$$

where $\alpha \equiv \dfrac{k_{on}}{\gamma_R}$. The term $\alpha \cdot m(t)$ describes the miRNA "efficacy"[1], which is the product of $\dfrac{k_{on}}{\gamma_R}$ and the miRNA level *m(t)*. Reduction of our time-dependent model to a steady-state model reduced two redundant fit parameters (*k_{on}* and γ_R) into one ($\alpha \equiv \dfrac{k_{on}}{\gamma_R}$) which supports our conclusion that the dynamics of lin-4 and *lin-14* interaction is indeed in the steady-state regime. In Eqn. [1], "fold-repression" thus appears as $1 + \alpha \cdot m(t)$. We directly used the moving-averaged *lin-14* mRNA concentration of *lin-14(n355gf)* animals (purple curve in Supplementary Fig. 13e) to infer $\dfrac{k_R(t)}{\gamma_R}$, since $\dfrac{k_R(t)}{\gamma_R} = u_{st}(t)$ given that $k_{on}(N = 0) = 0$ for this strain. To find $m(t)$, we again used our spline-fitted experimental measurement of mature lin-4 from *lin-14(n355gf)* animals (purple curve in Supplementary Fig. 13f). We then determined the value of $\alpha \equiv \dfrac{k_{on}}{\gamma_R}$ (in arbitrary unit, since *m(t)* is in arbitrary unit) by fitting our steady-state model $u_{st}(t)$ to our experimental data for *N* = 7 (wild-type, Supplementary Fig. 13g) and *N* = 2 (*lin-14(n536gf)*, Supplementary Fig. 13h).

The best fit values obtained were: *$k_{on}(N = 7)/\gamma_R$* = (1.66 ± 0.14) and *$k_{on}(N=2)/\gamma_R$* = (0.56 ± 0.09). Errors indicate 95% confidence intervals, which were obtained by Monte Carlo simulation (1,000

trials). From this result, we speculate that each of the LCE in *lin-14* 3'-UTR equally contributes to the overall strength of miRNA-target interaction, parameterized as k_{on} in our model (Fig. 4c).

What is the advantage of having miRNA synchronously expressed with its target for dampening cyclic target gene expression fluctuations? From Eqn. [1], we calculate the differential of $u_{st}(t)$

$$\Delta u_{st} = u_{st}(t) \cdot \left[\frac{\Delta k_R}{k_R(t)} - \left(\frac{\alpha \cdot m(t)}{1 + \alpha \cdot m(t)} \right) \cdot \frac{\Delta m}{m(t)} \right]$$

$$\frac{\Delta u_{st}}{u_{st}(t)} = \left[\frac{\Delta k_R}{k_R(t)} - \left(\frac{\alpha \cdot m(t)}{1 + \alpha \cdot m(t)} \right) \cdot \frac{\Delta m}{m(t)} \right]$$

$$G(u_{st}(t)) = G(k_R(t)) - \left(\frac{\alpha \cdot m(t)}{1 + \alpha \cdot m(t)} \right) \cdot G(m(t)) \qquad [2]$$

where *G* denotes the relative rate of change, or logarithmic gain[2]. Note that $G(u_{st}(t))$ is equal to the difference between $G(k_R(t))$ and $G(m(t))$ weighted by a function, which depends on $\alpha \cdot m(t)$. For the sake of simplicity, we will consider small relative changes so that we can let $\frac{\delta u}{u_{min}} \approx \frac{\Delta u_{st}}{u_{st}(t)}$, $\frac{\delta k_R}{k_{R\,min}} \approx \frac{\Delta k_R}{k_R(t)}$, and $\frac{\delta m}{m_{min}} \approx \frac{\Delta m}{m(t)}$. As we see from Eqn. [2], in the case of a miR-IFFL where the miRNA is synchronously expressed with its target, $\frac{\delta k_R}{k_{R\,min}}$ and $\frac{\delta m}{m_{min}}$ carry the same signs and thus $\frac{\delta m}{m_{min}}$ acts to cancel out the change that occurs to $\frac{\delta k_R}{k_{R\,min}}$. This results in a reduced $\frac{\delta u}{u_{min}}$ at all times. This becomes optimal when $\alpha \equiv \frac{k_{on}}{\gamma_R}$ carries a particular value. When this value is below the optimum, the performance falls in sub-optimal space which is lower left of the parameter space in Figure 7d, because the miRNA efficacy is not strong enough to completely eliminate the target level peaks. On the other hand, when this value is above the optimum, the performance falls in upper right part of the parameter space in Figure 7d. This seemingly counterintuitive case occurs when there is an "excess" damping where a miRNA pulse not only eliminates the target level peak but also creates a trough due to a strong repression, effectively generating a cyclic target expression level fluctuation with a 180° phase

shift (Supplementary Fig. 14). Interestingly, regardless of what $\alpha \equiv \dfrac{k_{on}}{\gamma_R}$ is, when miRNA

expression is constitutive ($\Delta m = 0$), $\dfrac{\delta u}{u_{min}}$ is not reduced (no damping).

**Supplementary Table 1: Assignment of genes to expression clusters for clusters genes.** A full list of gene assignments to co-expression clusters can be found in Supplementary Table Table 1 online. The table lists the gene ID, gene name (if available), wormbase gene ID, the expression cluster and information on RNAi phenotypes retrieved from wormbase (WS190).

Supplementary Table 2: A full list of GO terms enriched in clusters of co-expressed genes. A full list of GO terms enriched in clusters of co-expressed genes can be found in Supplementary Table 2 online. For each cluster, enriched biological processes and enriched molecular functions are given as separate lists. Only significantly enriched GO-terms ($P < 0.05$) comprising more than five genes are included. The lists indicate the GO-term ID, the hypergeometric P-value, the odds ratio, the expected number of genes associated with each GO-term, the observed number of genes for each GO-term, the size of the GO-term (total number of genes associated) and a short description. For the inference of over-represented GO terms, each cluster was compared to the universe of all clusters.
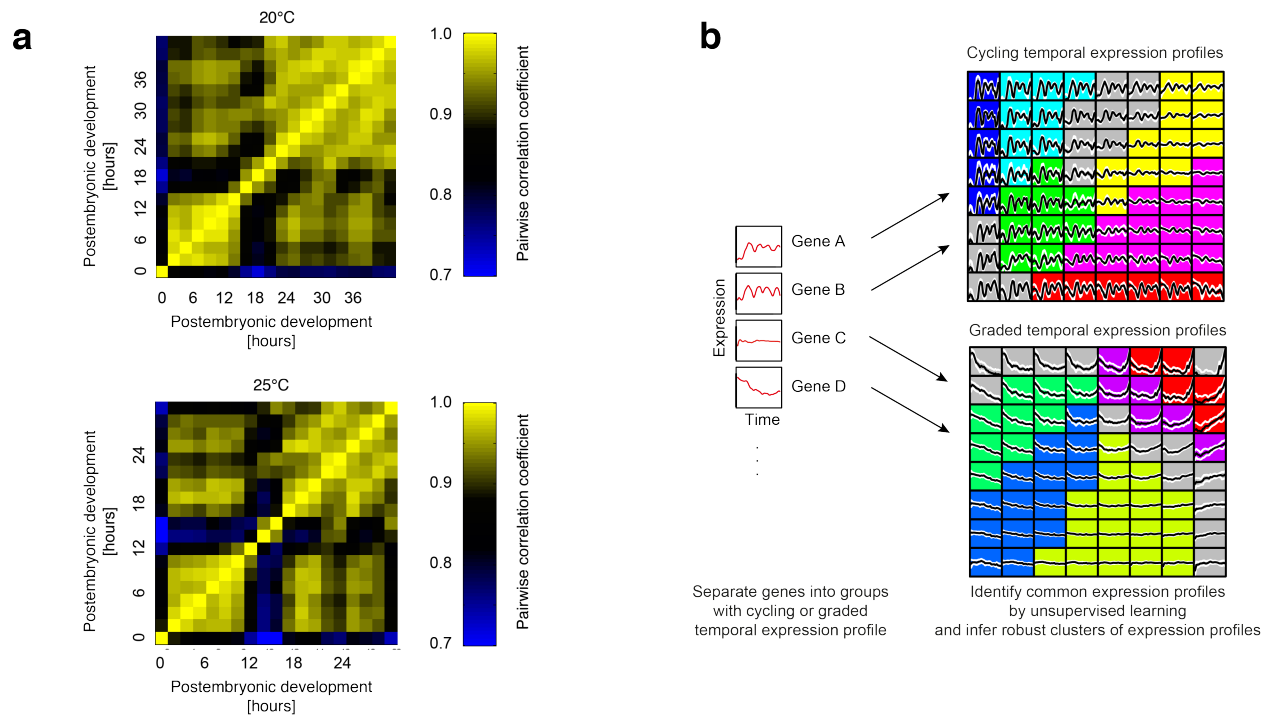
Supplementary Figure 1: Identification of clusters co-expressed transcripts during *C. elegans* transcripts larval development. (**a**) Pairwise correlation of transcriptomes between different developmental times determined at 20°C (upper panel) and 25°C (lower panel). (**b**) Genes with cycling temporal expression profiles (Durbin-Watson *P*<0.05) were separated from genes with graded temporal expression. To resolve distinct modes of expression within the groups of cycling and graded genes, we first eliminated relative shifts in expression profiles by normalizing expression of each gene with the sum of expression values over all time-points. We then created a self-organizing map[3] that projects the temporal expression profiles onto a two dimensional grid with only 20 x 20 grid-points (see Online Methods). Self-organizing maps are commonly used techniques for achieving visualization of high dimensional data and have previously been applied to classify expression data[4–6]. This method maps similar expression profiles to the same or neighboring grid points and reduces the full number of 16,776 profiles to 400 groups of profiles. On this reduced set we applied robust k-means clustering with 100 bootstraps to identify reproducible clusters of gene expression profiles (see Online Methods). The two-dimensional grids represent SOMs for each group and robust clusters of expression profiles are color-coded. Profiles that do not fall into a robust cluster are shown in grey. The average normalized expression profile (black line) and the standard deviation (white line) is shown for each point of the SOM.

a

All genes

Cycling genes

b

daf−7

nas−7

c

Cycling Genes
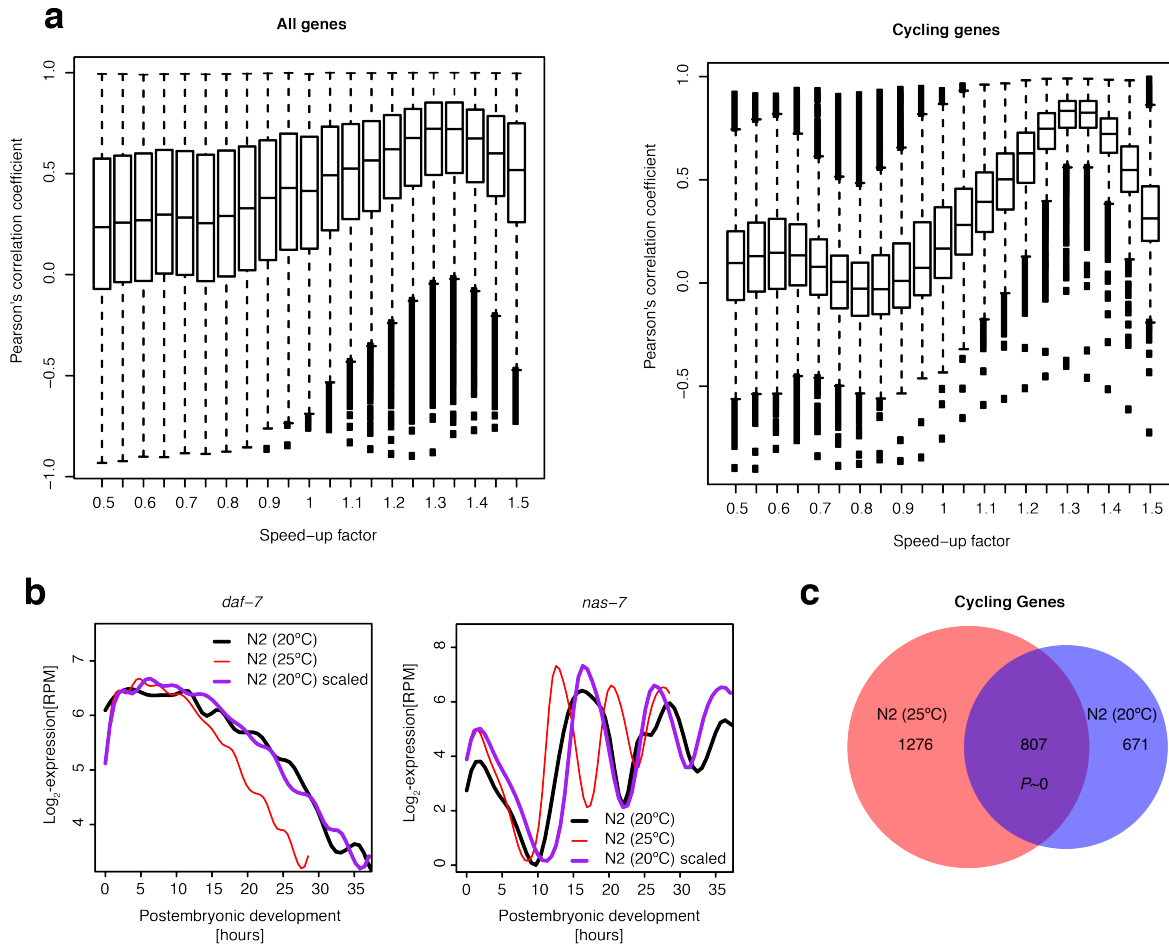
Supplementary Figure 2: Developmental time is accelerated at higher temperatures. To quantitatively measure the developmental speed-up at the higher temperature we rescaled developmental time at 25°C by a variable factor and computed the correlation between temporal gene expression profiles at 20°C and 25°C with rescaled time. (**a**) Expression profiles sampled every 1.5 hours during larval development at 25**°**C were rescaled by multiplying the time coordinate with a factor that takes a value between 0.5 and 1.5 in 20 discrete steps. The computation was performed using all genes (left) or using only cycling genes (right), which show a more pronounced effect. The genome-wide correlation average showed a clear peak after linear rescaling with a factor of 1.3 suggesting that at 25°C the developmental clock runs ~30% faster. Rescaling increases the average correlation from R=0.44 to R=0.72. Considering only cycling genes that could be conveniently used as a timer, yielded the same speed-up, but the correlation gain is even more pronounced (R=0.12 versus R=0.83). After rescaling, the correlation to the corresponding expression profile at 20**°**C was computed for each gene. The rescaling factor that yielded the maximum correlation was used as an estimate for the developmental speed-up. Boxes represent the interquartile range, the median is indicated by

the black horizontal line, whiskers indicate the 5%- and the 95%-quantile and outliers are shown as black squares. (**b**) The effect of rescaling developmental time is shown for two genes with a temporal gradient (left) or with oscillating expression (right). (**c**) The overlap of genes classified as cycling (Durbin Watson $P < 0.05$) at the two temperatures. Many genes have p-values close to 0.05 and small variations in the p-value explain the different classification at the two temperatures. The overlap is highly significant (P~0).
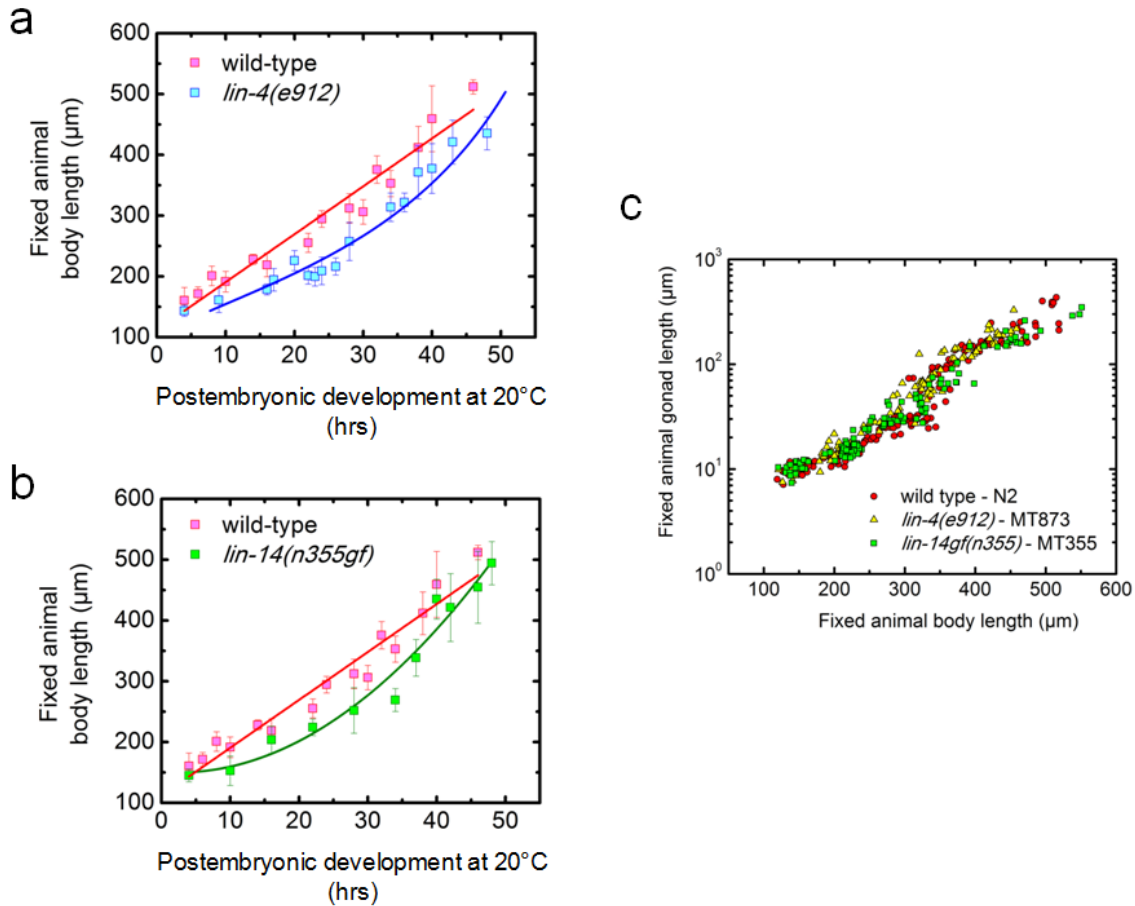
Supplementary Figure 3: Body length as a developmental age indicator. We found animal body length to be a robust developmental age indicator. **a**-**b**, We sampled the body lengths of animals grown on OP50 in 20°C from differently synchronized batches. Animals were synchronized by hypochlorite treatment. Body lengths of wild-types were overall longer than *lin-4(e912)* (**a**) and *lin-14(n355gf)* (**b**) mutants of the same developmental time, presumably because wild-types have higher growth rates[7]. We fitted these data to lines or curves to convert body lengths of different strains into developmental times. Note that we have used a linear correlation between body length and developmental time for wild-types to simplify our data analysis throughout this work (Supplementary Fig. 6). Error bars, s.d.; n > 10. **c**, Because the germ line and gonad of *lin-4* and/or *lin-14gf* mutant animals mature at similar rates as wild-types[7] and since (2) we found gonad length (distance between the two distal tip cells along the gonad arms) and body length of an animal to be identically correlated in wild-types, *lin-4* and *lin-14gf* mutants, we considered animals of the same body length to be at identical developmental age regardless of the mutation.

Mid-body intestinal cell binucleation
(1 - mononucleate / 2 - binucleate)

wild-type

lin-4(e912)

lin-14(n355gf)
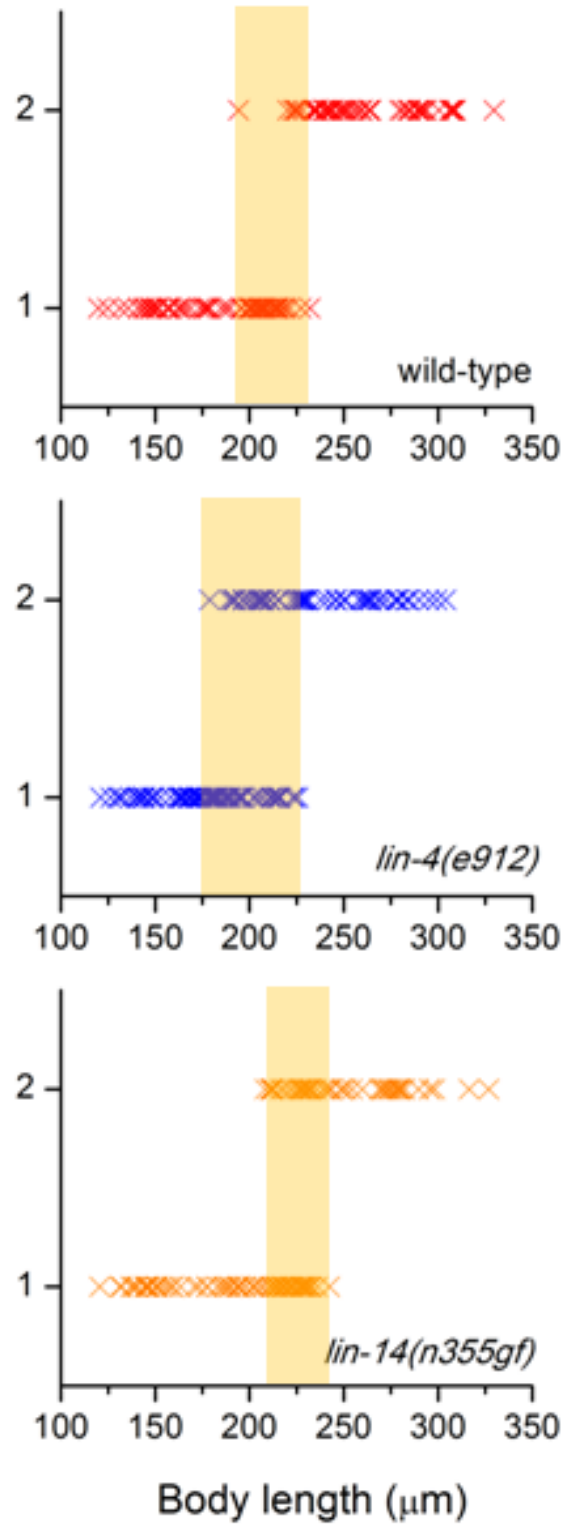
Body length (μm)

Supplementary Figure 4: The timing of binucleation of intestinal cells correlates with a range of animal body lengths. Intestinal nuclei in the mid-body region divide without cell division at the beginning of the lethargus prior to the first molt, which makes this binucleation event a useful developmental landmark for determining the age of an early stage animal[8]. When the nuclei are stained with DAPI, binucleated intestinal cells are clearly distinguishable from mononucleated cells. We fixed and stained wild-type, *lin-4(e912)* and *lin-14(n355gf)* animals with DAPI and simultaneously determined the nuclear state of intestinal cells and body length of individual animals, to test whether animal body length can be used as a proxy for early developmental ages. We found that intestinal binucleation occurs at the body length range (shaded in yellow) of 190µm~225µm in wild-types and 175µm~225µm in *lin-4(e912)* animals. In *lin-14(n355gf)* animals, this was shifted to 200µm~250µm which is consistent with the overall shift of *lin-14* mRNA expression dynamics compared to that of *lin-4(e912)* animals (Fig. 6a and Supplementary Fig. 11). Therefore, we can distinguish animals of at least three distinct developmental age groups within L1 stage based on body lengths – for instance, "before (<175µm)", "during (>175µm and <225µm)", and "after (>225µm)" intestinal binucleation of *lin-4(e912)* mutants in L1 stage. We can use this information to further support our conclusion from Figure 6a that *lin-14* mRNA expression levels are temporally "pulsatile", because the *lin-14* mRNA levels of animals "before" and "after" intestinal binucleation are clearly distinct from that of animals "during" intestinal binucleation (Fig. 6a).

Gonad arm reflection
(1 - before / 2 - after)

Anterior arm

Posterior arm

wild-type

lin-4(e912)

*lin-14(n355gf)*

Body length (μm)
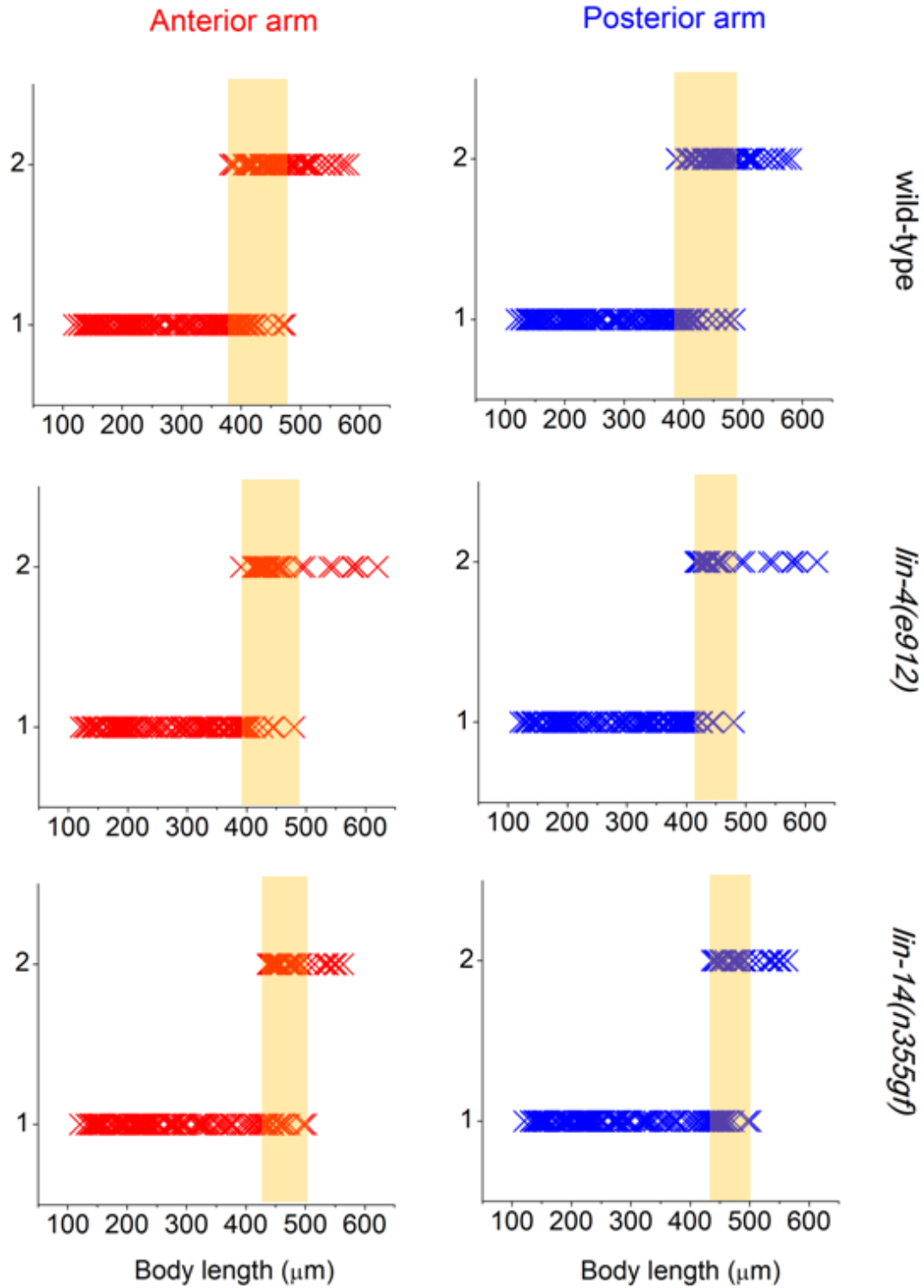
Body length (μm)

Supplementary Figure 5: The timing of gonad arm reflection correlates with animal body length. During postembryonic development, the anterior and posterior gonad arms elongate with the two distal tip cells located at the distal ends of the arms migrating away from each other. Around late L3 and L3 molt, both arms make reflecting turns and elongate towards each other[9]. Since *lin-4* and *lin-14* do not have any obvious effect on their development, gonad arm reflection is a useful developmental landmark for determining the age of a later stage animal. We fixed and stained wild-type, *lin-4(e912)* and *lin-14(n355gf)* animals with DAPI and simultaneously determined the gonad arm morphology and body length of individual animals, to again test whether animal body length can be used as a proxy for late developmental ages. We found that gonad arm reflection occurs at the body length range (shaded in yellow) of 390µm~475µm in wild-types and 400µm~475µm in *lin-4(e912)* animals. In *lin-14(n355gf)* animals, this was shifted to 440µm~500µm which is consistent with the overall shift of *lin-14* mRNA expression dynamics compared to that of *lin-4(e912)* animals (Fig. 6a and Supplementary Fig. 11). Therefore, we can distinguish animals of early, late L3 and early L4 stages based on body lengths.
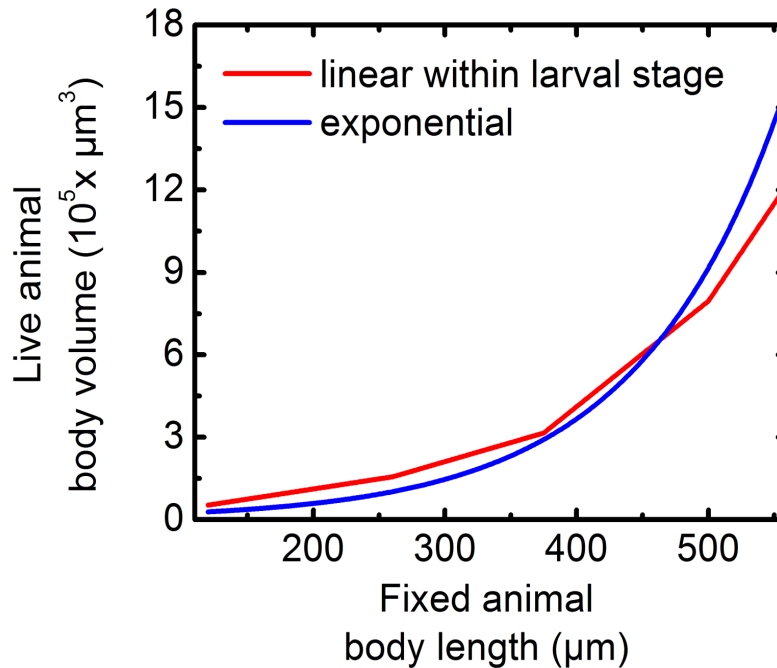
Supplementary Figure 6: Live animal body volume as a function of fixed animal body length. We used live wild-type animal volume data from Knight *et al*., 2002[10] to calculate *lin-14* mRNA concentration during post-embryonic development of *C. elegans*. Because the growth rates of L1-arrested synchronized animals are different from that of freely growing animals, we could not directly adopt the published result V=46.6*exp(0.0722*t) (V, in $\mu m^3 \times 10^3$ and t, in hrs). To correct for this, we first constructed a piecewise linear volume growth curve as a function of body length (red) using the larval stage specific constant growth rates described in Knight *et al*., 2002[10]. Given the linear correlation between body length and developmental time of wild-types (Supplementary Fig. 3), we were able to draw straight lines with constant slopes (growth rates) for each larval stage. Body lengths at which each larval stage transition occurred were estimated from collagen coding gene mRNA expressions. In our study, we used an exponential curve (blue) that fits well to the piecewise linear curve (red) to calculate *lin-14* mRNA concentration of each animal of a particular body length. The equation describing the blue curve is V=46.6 * exp(((8*L-893.2)/873.5)-0.578) (V, in $\mu m^3 \times 10^3$ and L in μm). We assumed animals with identical body length to have identical body volume regardless of the mutant background used in our study.
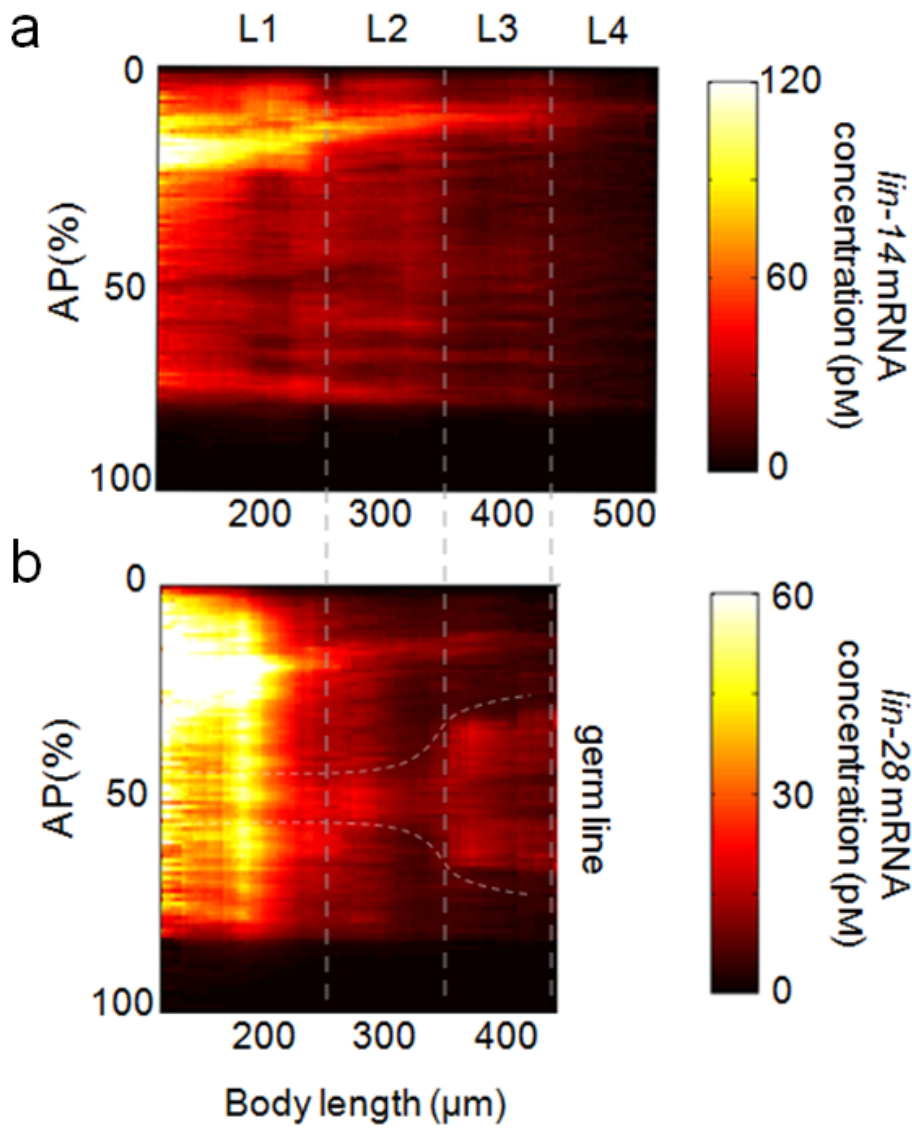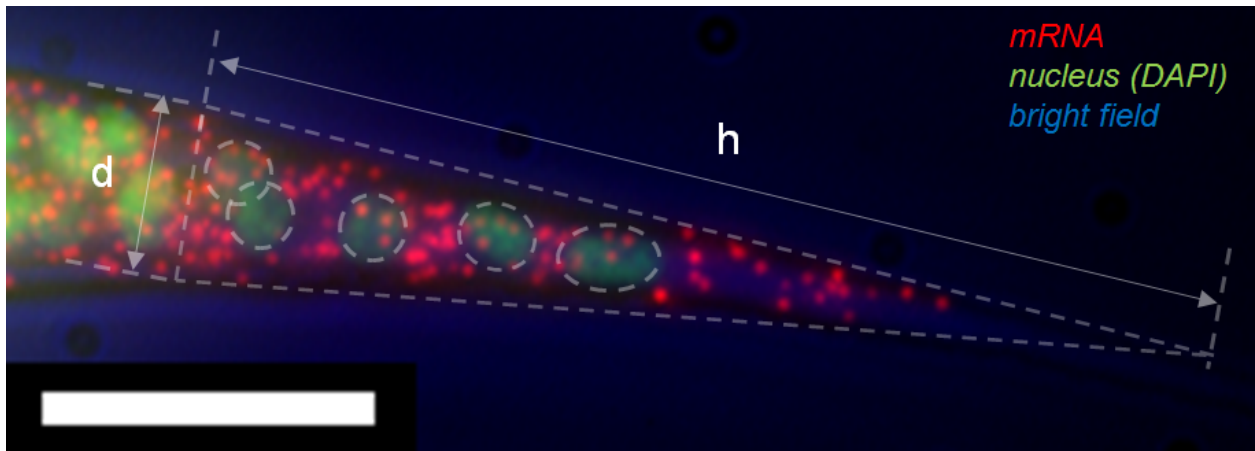
Supplementary Figure 7: AP mRNA concentration map for _lin-14_ (a) and _lin-28_ (b). AP(%) indicate relative position along AP axis (0%-head, 100%-tail). The height of each bin is 1% and a moving average (bin; 36µm) is applied in x-direction.
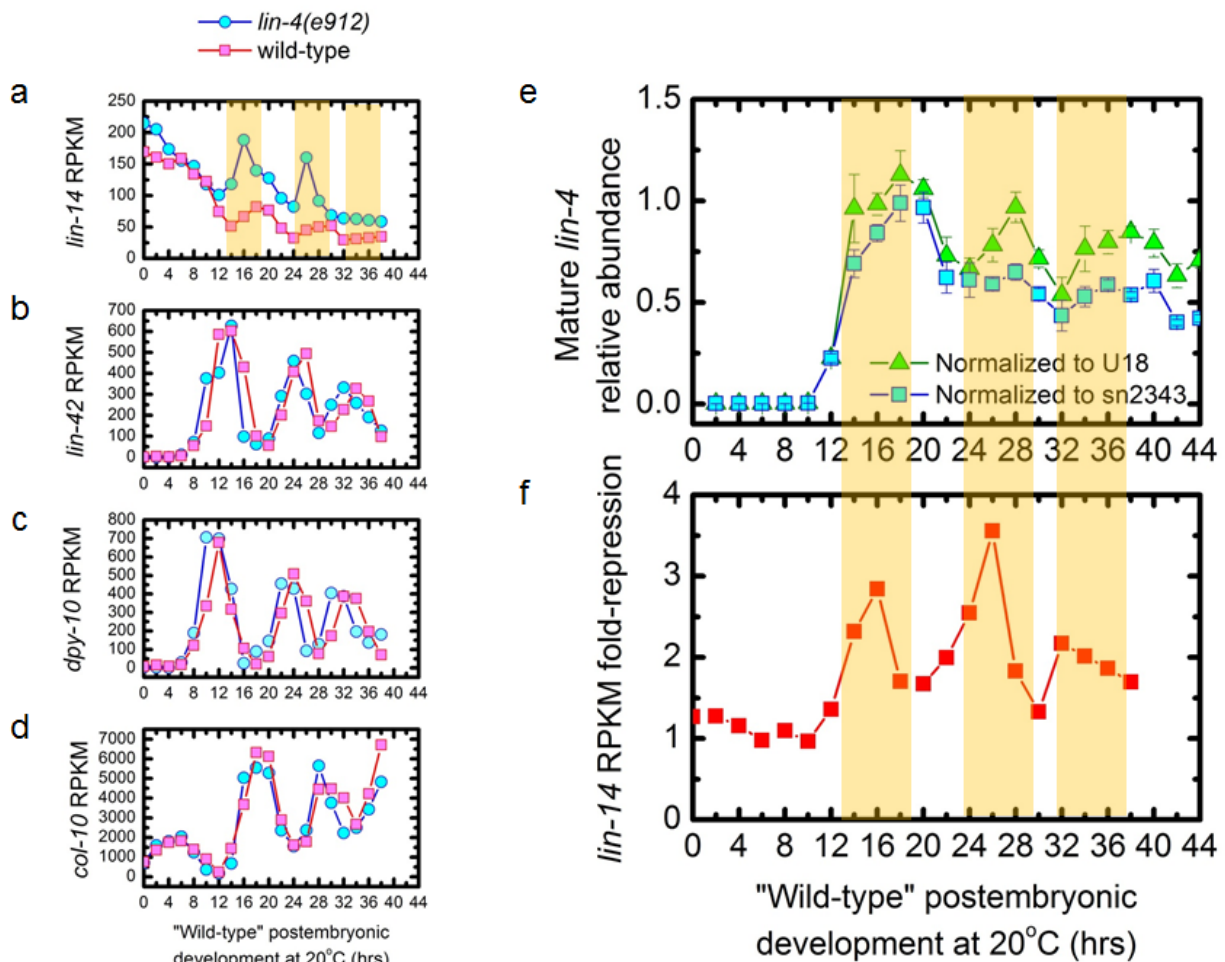
Supplementary Figure 8: RPKM dynamics of lin-4 targets and non-lin-4 targets in wild-type and *lin-4(e912)* KO animals. a-d, RPKM dynamics of *lin-14* (a), *lin-42* (b), *dpy-10* (c) and *col-10* (d). RNA-Seq experiments were also performed using poly(A)$^+$ RNA libraries prepared from synchronized *lin-4(e912)* KO mutant larval populations representing 25 different developmental time points ranging from 0 hr to 48 hr after hatching with 2 hr resolution at 20°C. This range spans the first three larval stages (L1, L2, and L3). Since the growth rates of the two strains (2 to 4hrs delay in *lin-4* mutants compared to wild-types) are different, the time axis of *lin-4* mutant RNA-Seq data was transformed in order to make direct comparison between wild-type and mutants. For proper transformation, genes that exhibit no significant difference between these strains (presumably these genes are neither targeted nor affected by lin-4), such as *lin-42*, *dpy-10 and col-10*, were used as references. Consistent with smFISH data in Figure

6a, RPKM levels of *lin-14* pulse in *lin-4* mutants (a). This strongly suggests that the pulsatile dynamics of *lin-14* in a *lin-4* mutant in Figure 6a is not caused by a FISH-specific or sampling artifact. **e**-**f**, Mean mature lin-4 miRNA level of wild-type larvae cultured at 20°C (e, also shown in Fig. 4a) and *lin-14* mRNA fold repression computed using the RNA-Seq data (shown in (a)) (f). Consistent with the smFISH data in Figure 6d, the timing of "fold-repression" peaks coincides with that of lin-4 expression peaks (yellow shaded regions in a, e and f).

a

mRNA
nucleus (DAPI)
bright field

b
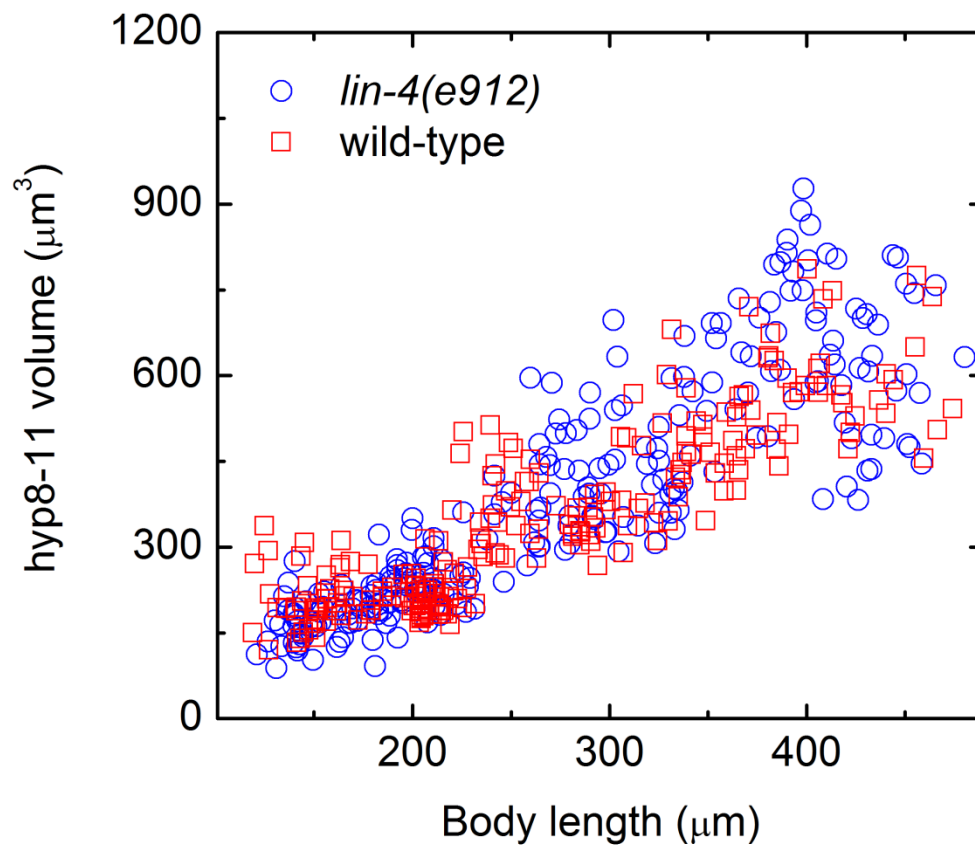
Supplementary Figure 9: Measuring mRNA concentration in the tail hyp8-11. a, Maximum Z-projection of mRNA FISH stack image in the tail tip. Single mRNA in red, DAPI labeled nuclei in green and bright field image in blue. Dashed circles outline the five hyp8-11 nuclei. Scale bar represents 10µm. hyp8-11 cells consist of five posterior-most nuclei in the tail tip. We assumed the geometry of hyp8-11 to be conical and determined its volume (v) by measuring the height (h) and base diameter (d) ($v = \frac{\pi \cdot h \cdot d^2}{12}$). Position of the cone's base was determined as the mid-point between the fifth and sixth posterior-most nuclei in the tail stained with DAPI (green). The height (h) was determined from bright field image of individual animal (blue). Only mRNA molecules (red) in the hyp8-11 cone were counted for concentration measurement (Fig. 6b). **b**, Volume of hyp8-11 cells as a function of body length in *lin-4(e912)* and wild-type animals appears to be similar.
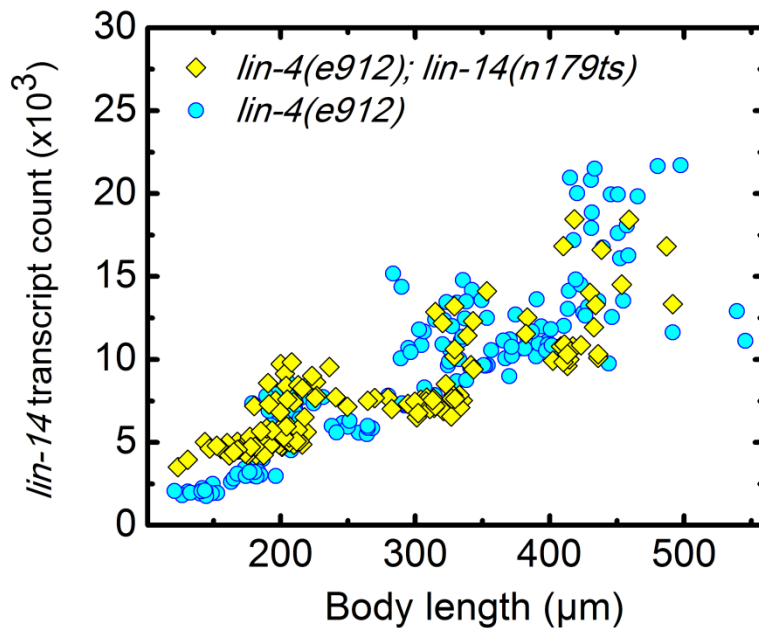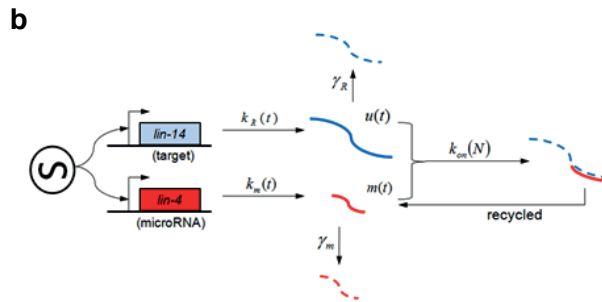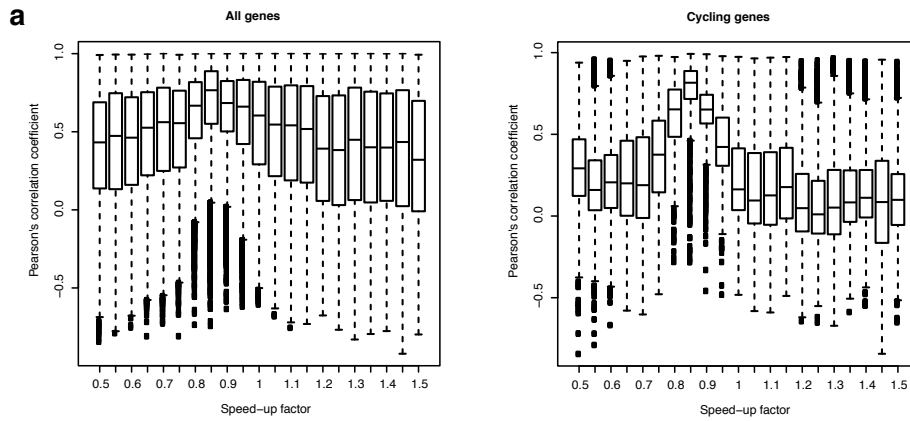
Supplementary Figure 10: Pulsatile expression of *lin-14* is not L1 specific. A phenotypic feature of *lin-4(e912)* and *lin-14(n355gf)* animals is that they exhibit reiterating L1 fates (hatch→L1→L1→L1→)[7,11], thus it is possible that either the oscillatory *lin-14* transcript levels are merely a repetition of pulses implemented by an upstream regulator that is L1 fate specific. To examine these possibilities, we counted *lin-14* transcripts in *lin-4(e912); lin-14(n179ts)* animals. *lin-14(n179ts)* is a temperature-sensitive loss-of-function allele[11]. As a consequence, these animals exhibit a "precocious" phenotype by skipping the L1 specific larval program (hatch→L2→L3→L4→)[11] at a restrictive temperature of 25°C. We can reliably quantify *lin-14* transcription activity because the *lin-14(n179ts)* mutation is not a nonsense mutation[12] and therefore escapes nonsense mediated decay[13]. We found that *lin-14* transcript levels are nevertheless puslatile in *lin-4(e912); lin-14(n179ts)* animals similar to the observed oscillations in *lin-4(e912)* animals, suggesting that *lin-14* oscillations are not caused by a L1 specific program.
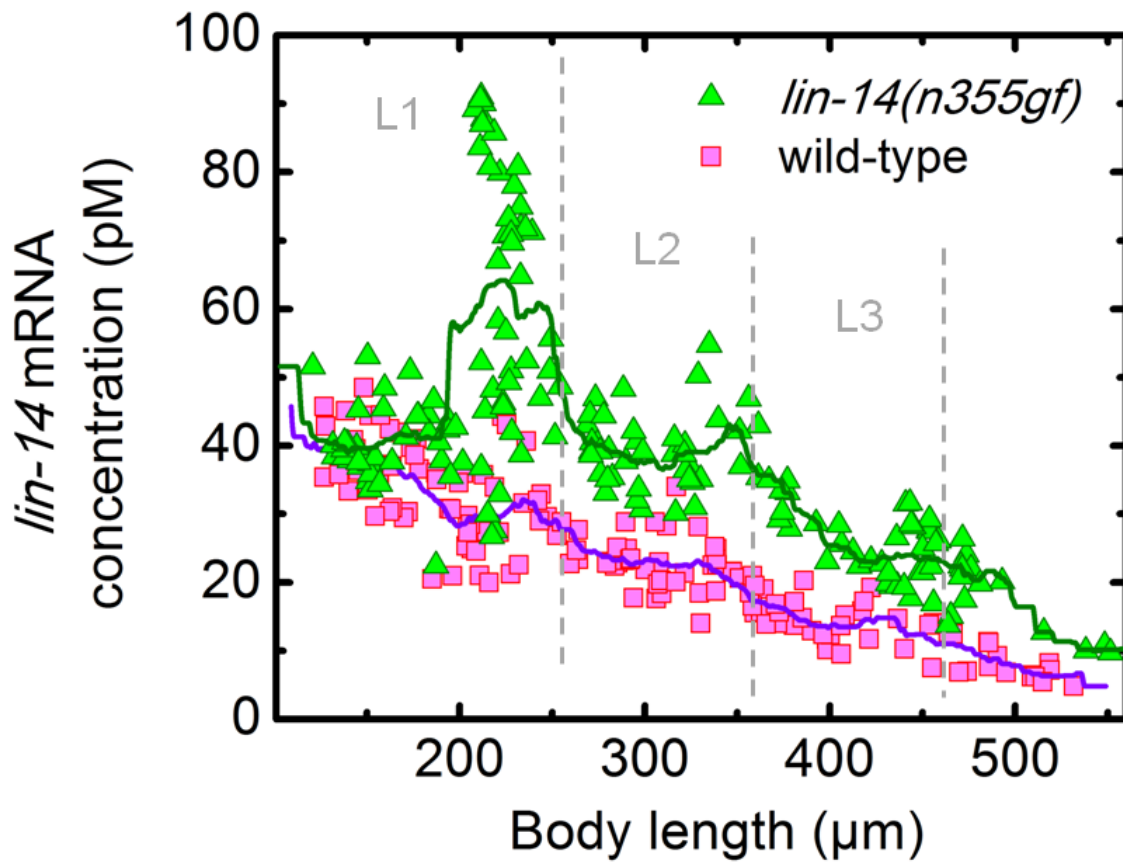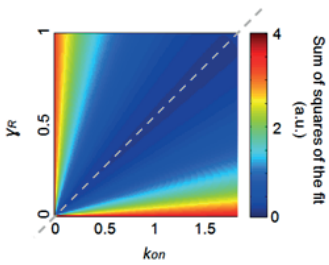
Supplementary Figure 11: *lin-14* **mRNA expression in** *lin-14(n355gf)* **mutants.** Curves indicate simple moving averages of the corresponding data points within a bin of size 36 μm. Wild-type data were shown for comparison. Dashed lines separate larval stages.
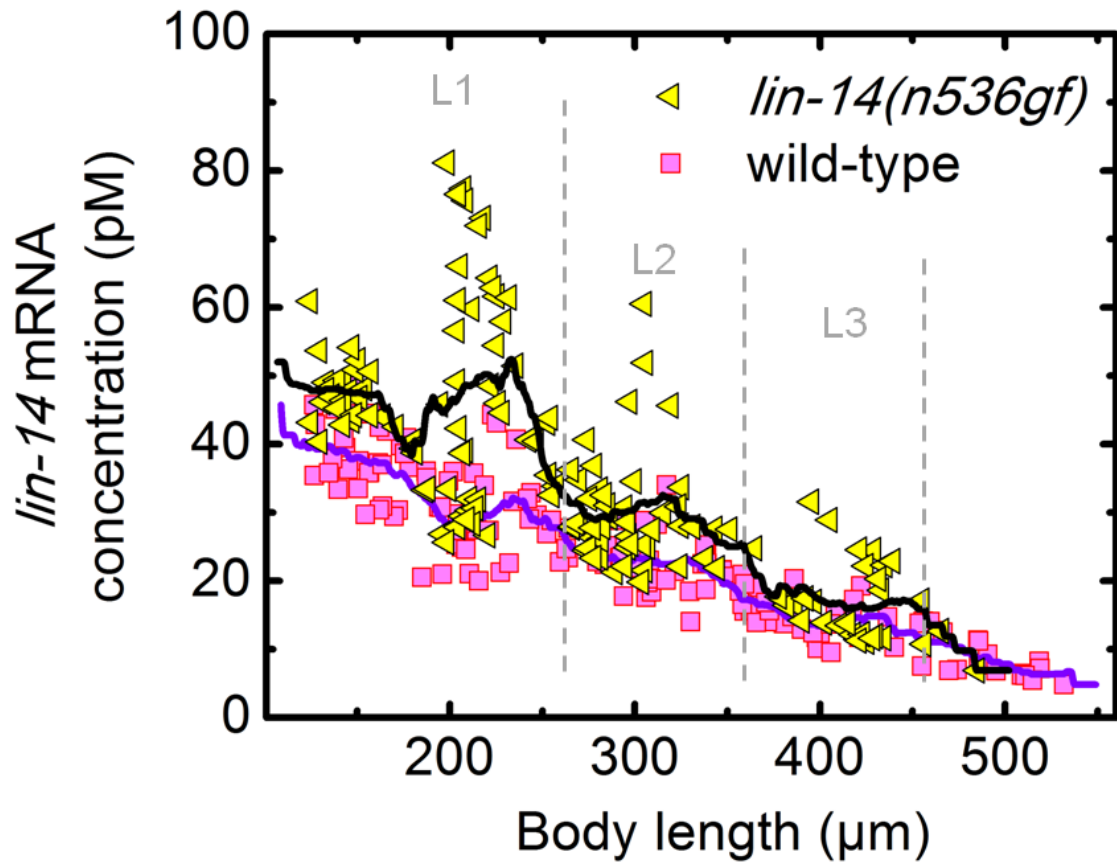
Supplementary Figure 12: *lin-14* **mRNA expression in** *lin-14(n536gf)* **mutants.** Curves indicate simple moving averages of the corresponding data points within a bin of size 36 μm. Wild-type data were shown for comparison. Dashed lines separate larval stages.
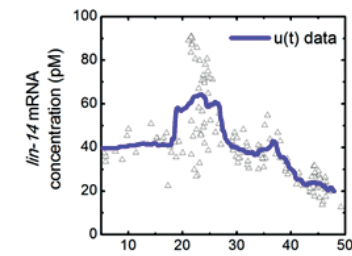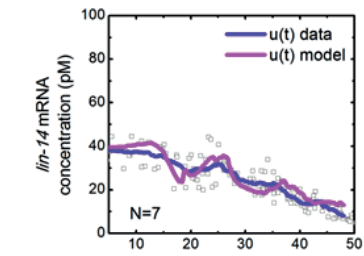
a

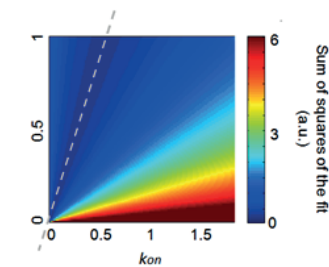All genes | Cycling genes
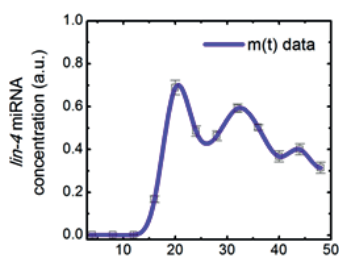
Pearson's correlation coefficient vs Speed–up factor

b

γ_R

$k_R(t)$ — $u(t)$

$k_{on}(N)$

lin-14 (target)

lin-4 (microRNA)

$k_m(t)$ — $m(t)$

recycled

γ_m

c $N=7$ (wild-type)

γ_R vs k_{on}

Sum of squares of the fit (a.u.)

e

lin-14 mRNA concentration (pM)

— $u(t)$ data

g

lin-14 mRNA concentration (pM)

— $u(t)$ data
— $u(t)$ model

$N=7$

d $N=2$ (*lin-14(n536gf)*)

k_{on}

Sum of squares of the fit (a.u.)

f

lin-4 miRNA concentration (a.u.)

— $m(t)$ data

h

lin-14 mRNA concentration (pM)

— $u(t)$ data
— $u(t)$ model
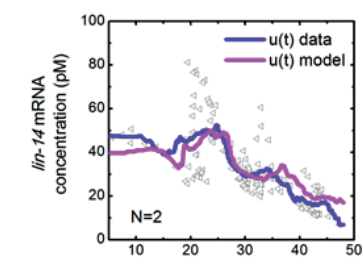
$N=2$

24

Supplementary Figure 13: Steady-state miR-IFFL model and data fitting. (**a**) Derivation of developmental timing difference between *lin-4(e912)* and wild-type animals. Expression profiles sampled from *lin-4(e912)* animals every 2h at 20°C were rescaled by multiplying the time coordinate with a factor that takes a value between 0.5 and 1.5 in 20 discrete steps. After rescaling, the correlation to the corresponding wild-type expression profile at 20°C was computed for each gene. The rescaling factor that yielded the maximum correlation was used as an estimate for the developmental speed-up. In *lin-4(e912)* animals, this factor equals 0.85 indicating a slower development than in wild-type animals. The computation was performed using all genes (left) or using only cycling genes (right), which show a more pronounced effect. Boxes represent the interquartile range, the median is indicated by the black horizontal line, whiskers indicate the 5%- and the 95%-quantile and outliers are shown as black squares. (**b**) A mathematical model to characterize the dynamics of target gene level u in the presence of miRNA level m. We assumed a time-variant production of the target mRNA $k_R(t)$ and miRNA $k_m(t)$, with decays described by first-order constant rates γ_R and γ_m respectively. We also assumed irreversible second-order miRNA-mediated target transcript degradation kinetics with a rate constant k_{on}. The rate k_{on} depends on the strength of the miRNA-target interaction which is proportional to the number of miRNA complementary elements N of the target transcript. (**c-d**) Sum of squares of the time-dependent model fit to the experimental data for various k_{on} and γ_R. Dashed gray curves indicate regions in the parameter space with the smallest sum of squares. $N = 7$ (wild-type) (**c**) and $N = 2$ (*lin-14(n536gf)* (**d**). (**e**) Moving-averaged *lin-14* mRNA concentration of *lin-14(n355gf)* animals (purple curve). (**f**) Spline-fitted qPCR measurement of mature lin-4 from *lin-14(n355gf)* animals (purple curve). Error bars represent standard deviation (n>3). (**g-h**) The best fit of our steady-state model $u_{st}(t)$ to our experimental data for $N = 7$ (wild-type) (**g**) and $N = 2$ (*lin-14(n536gf)* (**h**).
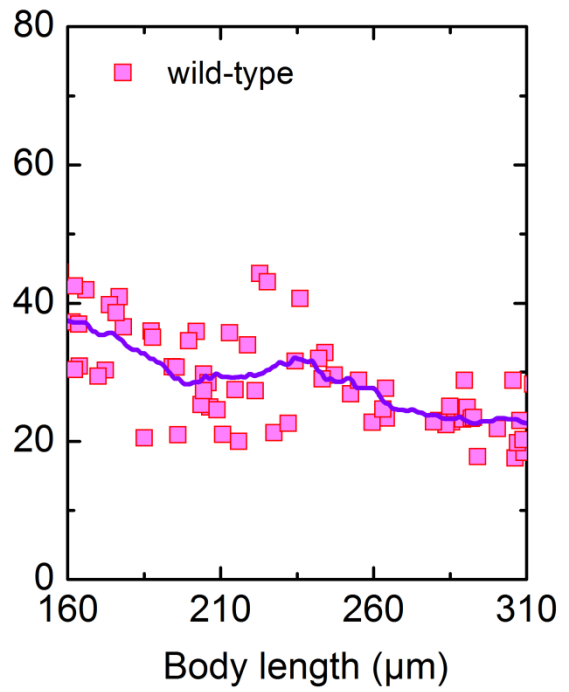
a
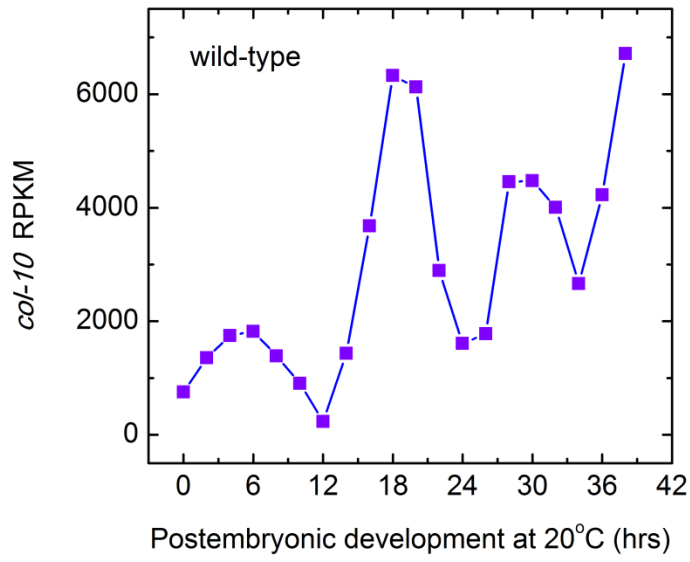
b
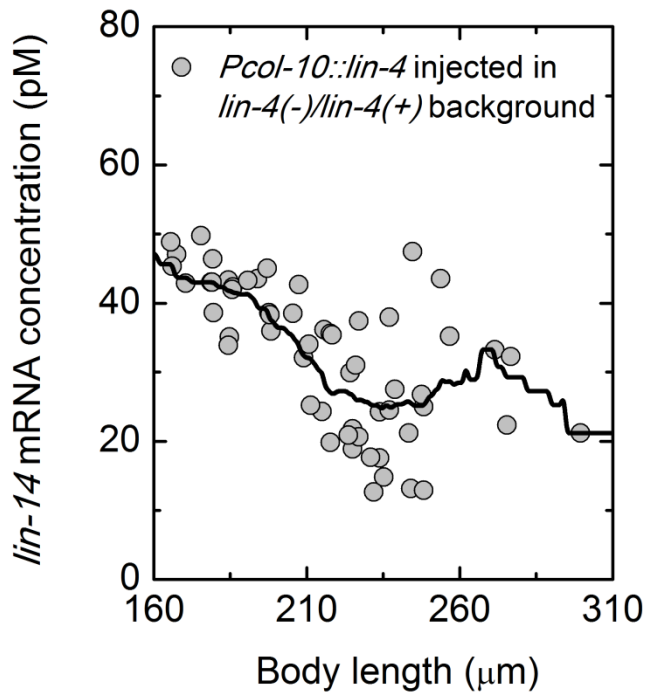
c

Supplementary Figure 14: *lin-14* **mRNA expression is over-damped when lin-4 miRNA is over-expressed.** Our model described in Supplementary Information predicts that the miRNA "efficacy" $\alpha \cdot m(t)$, where $\alpha \equiv \dfrac{k_{on}}{\gamma_R}$, is optimally balanced in wild-types. To explore suboptimal conditions, namely the upper right corner of the miR-IFFL performance parameter space in Fig. 7d, we asked how *lin-14* mRNA expression dynamics would change when lin-4 miRNA is over-expressed. *col-10* is a molting gene that is known to be expressed periodically at high levels in the hypodermal tissue and from our RNA-Seq data (**a**) we found its oscillatory phase to be identical to that of lin-4 miRNA expression (Fig. 4a). We measured *lin-14* mRNA levels in animals expressing *Pcol-10::lin-4* (pHZ081) in a balanced *lin-4(e912)/mC6* II background[14]. Animals were grown in 23°C to select for co-injection marker *pha-1(+)*. We excluded animals that lost *mC6* balancer by analyzing only the animals expressing gfp (*mC6* carries gfp) so that the synchronous expression of a single endogenous *lin-4* locus and transgene *Pcol-10::lin-4* will increase peak heights of lin-4 miRNA level. The result would be increased relative fluctuations in lin-4 miRNA level, leading to an over-damping of *lin-14* mRNA levels according to our model's prediction. This is equivalent to shifting the N=7 asterisk to the right hand side across the dark blue valley in Figure 7d. Although the *col-10* promoter is active only in the hypodermal tissue, it makes up a large fraction of the total animal volume and we indeed observed a transient decrease in the total number of *lin-14* mRNA in these transgenic animals of body lengths 210μm - 250 μm (**b**) compared to the smooth dynamics seen in wild-types (**c**). Curves in **b**-**c** indicate simple moving averages of the corresponding data points within a bin of size 36 μm.

References

1. Larsson, E., Sander, C. & Marks, D. mRNA turnover rate limits siRNA and microRNA efficacy. *Mol. Sys. Biol.* **6**:433 (2010).

2. Savageau, M. A. Parameter sensitivity as a criterion for evaluating and comparing the performance of biochemical systems. *Nature* **229**, 542-544 (1971).

3. Kohonen, T. Self-organized formation of topologically correct feature maps. *Biological Cybernetics* **43**, 59-69 (1982).

4. Jiang, M. *et al.* Genome-wide analysis of developmental and sex-regulated gene expression profiles in *Caenorhabditis elegans*. *Proc. Natl. Acad. Sci. USA* **98**, 218-223 (2001).

5. Kim, S.K. *et al.* A gene expression map for *Caenorhabditis elegans*. *Science* **293**, 2087-2092 (2001).

6. Spencer, W.C. *et al.* A spatial and temporal map of *C. elegans* gene expression. *Genome research* **21**, 325-341 (2011).

7. Ambros, V. & Horvitz, H. Heterochronic mutants of the nematode *Caenorhabditis elegans*. *Science* **226**, 409-416 (1984).

8. Hedgecock, E.M. & White, J.G. Polyploid tissues in the nematode *Caenorhabditis elegans*. *Dev. Biol.* **107**, 128-133 (1985).

9. Hirsh, D., Oppenheim, D. & Klass, M. Development of the reproductive system of *Caenorhabditis elegans*. *Dev. Biol.* **49**, 200-219 (1976).

10. Knight, C.G., Patel, M.N., Azevedo, R.B.R. & Leroi, A.M. A novel mode of ecdysozoan growth in *Caenorhabditis elegans*. *Evolution & development* **4**, 16-27 (2002).

11. Ambros, V. & Horvitz, H.R. The *lin-14* locus of *Caenorhabditis elegans* controls the time of expression of specific postembryonic developmental events. *Genes & Development* **1**, 398-414 (1987).

12. Reinhart, B.J. & Ruvkun, G. Isoform-specific mutations in the *Caenorhabditis elegans* heterochronic gene *lin-14* affect stage-specific patterning. *Genetics* **157**, 199-209 (2001).

13. Pulak, R. & Anderson, P. mRNA surveillance by the *Caenorhabditis elegans smg* genes. *Genes & Development* **7**, 1885-1897 (1993).

14. Zhang, H. & Fire, A.Z. Cell autonomous specification of temporal identity by *Caenorhabditis elegans* microRNA *lin-4*. *Dev. Biol.* **344**, 603-610 (2010).